Check for updates

An optical sensing platform for the detection of anti-cancer drugs and their cytotoxicity screening using a highly selective phosphorene-based composite†

Nasrin Sultana, [ID] [a,b] Chingtham Thanil Singh, [ID] [a,b] Mojibur R. Khan[a,b] and Neelotpal Sen Sarma [ID] *[a,b]

Monitoring therapeutic drugs and their elimination is crucial because they may cause severe side effects on the human body. Methotrexate (MTX) is a widely used anti-cancer drug, which is highly expensive, and the detection of unwanted overdoses of MTX using traditional procedures is time-consuming and involves complex instrumentation. In this work, we have developed a nanocomposite material using phosphorene, cystine, and gold (Ph−Cys−Au) that shows excellent optical properties. This nanocomposite can be used as an optical sensing platform for the detection of MTX in the range 0−260 μM. The synthesized sensing platform is very sensitive, selective, and cost-effective for the detection of MTX. Ph−Cys−Au can effectively detect MTX in aqueous media with a limit of detection (LOD) of about 0.0266 nM (for a linear range of 0−140 μM) and 0.0077 nM (for a linear range of 160−260 μM). The nanocomposite is equally selective for real samples, such as human blood serum (HBS) and artificial urine (AU) with a LOD of 0.0914 nM and 0.0734 nM, respectively. We have also determined the limit of quantification (LOQ); the LOQ values for the aqueous media were 0.0807 nM (for a linear range of 0−140 μM) and 0.0234 nM (for a linear range of 160−260 μM), whereas, the values for HBS and AU were around 0.2771 nM and 0.2226 nM, respectively. Moreover, the nanocomposite also provides a feasible platform for cytotoxicity screening in cancerous cells (Caco-2 cell lines) and non-cancerous cells (L-929 cell lines).

1. Introduction

Effective clinical care is essential to be provided to patients who suffer from severe diseases and therefore there is a need for therapeutic drug monitoring (TDM) analysis. TDM involves the measurement of medication levels in the blood of humans to avoid toxicity resulting from the underdosing or overdosing of drugs.[1] It mainly focuses on drugs with a narrow therapeutic range. To improve efficiency and decrease adverse side effects, it is suggested to monitor the drug with a narrow therapeutic window and significant pharmacokinetic variance. Therefore, there is a need for reliable, easy, and spot detection methods to minimize the side effects of such drugs. The World Health Organization listed methotrexate (MTX, namely 2,4-diamino-*N*-10-methyl folic acid) as one of the most essential anti-cancer and anti-folate drugs. When administered into

the human body, it interferes with folic acid metabolism and leads to the blockage of *de novo* nucleotide synthesis, protein production, and cell proliferation.[2] For the treatment of various carcinomas, such as breast, gastric, head, and neck cancers; acute lymphoblastic leukaemia (ALL); osteosarcoma; and choriocarcinoma, body surface area-based doses higher than 500 mg m^{-2} of MTX (denoted as HD-MTX) are given intravenously.[3] It takes 1–2 hours to be absorbed inside the body once administered. Since MTX is highly toxic, it can prevent the growth of healthy cells, which limits its clinical recommendations. The most frequent cancer in children is acute lymphoblastic leukaemia, representing 25% of the malignancies where HD-MTX is crucial for the treatment.[1,4] However, systemic toxicity and acute nephrotoxicity are the two main side effects of HD-MTX therapy.[5] The MTX value of more than 10 μM in blood plasma is very dangerous for a period of 10 hours. This increase in the MTX level in blood results in some severe diseases, such as poisoning effects to the lungs, ulcers of the stomach, and heart stroke.[6]

Considering all these issues, the development of fast and sensitive detection methodologies is required. The low safety window of MTX makes it necessary to monitor its therapeutic

[a]Institute of Advanced Study in Science and Technology, Paschim Boragaon, Guwahati-35, Assam, India. E-mail: neelot@iasst.gov.in

[b]Academy of Scientific and Innovative Research (AcSIR), Ghaziabad-201002, India

levels in the human body. There are several analytical methods for detecting MTX, such as surface plasmon resonance, surface-enhanced Raman scattering, high-performance liquid chromatography, electrolysis, immunoassays, radioimmuno-assay, enzyme-multiplied immunoassay, protein binding, enzyme inhibition, microbiological assays, and electro-chemical assays.[1,3,7–10] In general, the high-pressure liquid chromatography (HPLC) method has been used to measure MTX in blood samples. The main disadvantage of these techniques is they are very complex and costly. These difficulties limit their use in rapid on-the-spot detection due to the employment of sophisticated and expensive instruments, complex sample preparation, and long analysis time.[11] Therefore, there is a need to develop methods that are cost-effective, sensitive, and capable of detecting MTX on the spot. Compared to the techniques outlined earlier, the fluorescence technique has achieved a lot of attention because of the rapid response, remarkable sensitivity, easy operation method, low toxicity, and the ability to detect non-destructively.[12,13] There are reports based on the fluorescence sensing of MTX.[14,15] Fluorescence methods can be considered as one of the efficient tools to understand different fields in a better way. The main capability of fluorescence-based sensors is that of 'seeing is believing'. The well-known mechanisms for the fluorescence-based sensing phenomenon are aggregation-induced emission (AIE),[16] Förster Resonance Energy Transfer (FRET),[17] inner filter effect (IFE),[18] ratiometric detection,[19] and photo-induced electron transfer (PET).[20] Among all the methods, FRET is potentially more powerful as it effectively responds to the analytes by changing their colour, brightness, lifetime, as well as anisotropy. This kind of analytical method can be carried out in real-time, is mostly free of different developing steps, including enzymatic amplification and washes, and is also suitable for intracellular sensing.[21] However, there are many fluorescence-based reports where researchers have used different 2D materials such as graphene, organic polymers, metal–organic frameworks (MOFs), covalent organic frameworks (COFs), MoS_2, WS_2, TMDs, etc.[22–24] All these materials involve hazardous chemicals, the synthetic procedures are time-consuming, and all have limited uses due to their production procedures. Therefore, a quick, sensitive, and affordable sensor system made of eco-friendly materials is required to overcome such difficulties.

Phosphorene (Ph) is considered one of the most versatile platforms among all the formerly evolved two-dimensional materials, due to its fascinating properties. It is a mono-elemental 2D material made up of phosphorus atoms obtained from the delamination of bulk black phosphorus (BP). BP has a layered structure with SP^3 hybridization. The BP nanosheets are held together by van der Waals interactions, and the interlayer spacing is about 0.53 nm. It possesses many unique electrical, optical, and electro-chemical properties. It also shows high carrier mobility, mechanical strength, biocompatibility, and high tensile strength, which make it efficient for different applications ranging from biomedical to electronic device fabrication. One of the important features of Ph is its band gap

tunability, which enables the fabrication of prototype devices that can be useful for different fields such as field effect transistors, batteries, solar cells, transistors, etc.[25] It also shows significant molecular absorptivity[26] and is known to have low cytotoxicity, which is suitable for fabricating sensors for healthcare applications.[27–34]

However, Ph is very sensitive to air. There are different strategies for stabilizing Ph by modification, such as molecular modification and ionic modification using different molecules and ions. Therefore, we aimed to develop a composite that stabilizes phosphorene and enhances its properties.[35] In our earlier work, we have seen that functionalization, as well as the reduction of phosphorene, may lead to the enhancement of its physical and chemical properties and can thus be applied to diverse fields. In this work, for the first time, we have successfully synthesized a composite of phosphorene-cystine-gold (Ph–Cys–Au) using a simple one-step hydrothermal approach. The notable optical properties of the synthesized nanoparticles inspired us to develop some fluorescence-based sensors for the detection of MTX. The designed biosensor displays different advantages such as sensitivity, selectivity, and cost-effectiveness and can detect MTX in real samples such as human blood serum and artificial urine. We believe that the development of such an innovative sensor with high selectivity as well as sensitivity can have a significant impact on the research community for the detection of MTX.

Apart from optical properties, we have also analyzed the cytotoxicity of the synthesized material as well as the composite of the material and MTX. To check the cytotoxicity, we used Caco-2 (human colorectal adenocarcinoma) and L-929 (mouse fibroblast) cell lines. The methyl thiazolyl tetrazolium (MTT) assay has been used to assess the cytotoxicity.

2. Experimental section

2.1 Materials and methods

2.1.1 Materials. The precursor materials for the synthesis of BP were red phosphorus (red P), tin powder, iodine, tin iodide (SnI_4), and tin. Red P, tin powder, iodine, and SnI_4 were purchased from Chempur. For the synthesis of Ph–Cys–Au nanodots, tin, and gold were purchased from Heraeus, and cystine and $HAuCl_4$ were obtained from SRL. Human colorectal adenocarcinoma cells (Caco-2) and mouse fibroblasts (L-929) were purchased from the National Centre for Cell Science (NCCS), Pune, India. Caco-2 and L-929 cells were maintained in Dulbecco's Modified Eagle's Medium (DMEM), (Gibco™, Cat. No.11965092), 10% fetal bovine serum (FBS) (Gibco™, Cat. No.16140089) with 1% pen/strep (Gibco™, Cat. No. 15070063) at 37 °C with 5% CO_2. The growth media were changed every alternate day. Thiazolyl blue tetrazolium bromide/MTT (Sigma, Cat. no. M2128) and dimethyl sulfoxide (DMSO) (Sigma, Cat. no. D8418) were purchased from Sigma-Aldrich, France. The human blood serum used in this study was purchased from Sigma-Aldrich (product code: H4522-

20ML). All the syntheses were carried out using deionized water.

2.1.1.1 Synthesis of black phosphorous (BP). For the synthesis of mineralizer SnI_4, tin powder (1.2 g, 99.995%, Chempur) and iodine (4.0 g, resublimed, 99.999%, Chempur) were mixed in 25 mL of toluene. The obtained solution was then refluxed for about 30 minutes until the violet colour of the iodine disappeared, which was followed by decantation. The resultant crystallized product was recrystallized with the help of toluene and was allowed to dry at room temperature.

Gold-stannane (AuSn) was prepared using gold and tin in a sealed, air-free silica ampoule. To melt down the starting material, an H_2/O_2 burner was used.

Next, 500 mg of Red P and 348 mg of AuSn were placed in a silica ampoule with an inner diameter of 10 mm and a length of 10 cm to synthesize BP, and after that, SnI_4 was added into the same ampoule. The ampoule was then evacuated to a pressure below 10^{-3} mbar and sealed with a H_2/O_2 burner. The ampoule was then heated for 3 h at 673 K inside a muffle furnace, followed by maintaining the temperature at 873 K for 23 hours. It was then cooled to 773 K with a cooling rate of 40 K h^{-1} and maintained there until the completion of the reaction. The ampoule was then allowed to cool at room temperature within 4 h, which led to the formation of BP crystals.[36]

2.1.1.2 Synthesis of phosphorene and Ph–Cys–Au nanodots. The dispersion of 2D BP followed by sonication-assisted liquid-phase exfoliation in an ice bath led to the formation of phosphorene (Ph). In a round-bottom flask, 100 mL of deionized water was taken, which was then bubbled with nitrogen for 10 minutes to eliminate the dissolved oxygen. To this, 20 mg of BP crystals were added after grinding using a mortar and pestle and the flask was sealed immediately. The mixture was then sonicated for about 8 hours in an ice bath. The prepared solution contained homogeneous 2D few-layer BP (FLBP) nanosheets or phosphorene (Ph).[37]

Ph–Cys–Au nanodots were synthesized by adopting a previously reported hydrothermal procedure with a minor modification.[38] Firstly, 20 mL of Ph (0.1 M) and 2 mL of cystine (0.1 M) were mixed in a beaker and stirred for about 30 minutes. After that, 1 mL of $HAuCl_4$ solution and a few drops of $NaBH_4$ were added and stirred for another 30 minutes using a magnetic stirrer. The obtained purple solution was poured into an autoclave and then placed in a hydrothermal reactor chamber and heated to 165 °C for 15 hours. The following scheme depicts the synthetic pathway of the nanocomposite (Scheme 1)

2.1.1.3 Assessment of cytotoxicity. For the cytotoxicity assay, Caco-2 and L-929 cells were seeded in 96-well plates at 1×10^4 viable cells per mL and incubated overnight. The cells were then treated with a culture medium containing different concentrations of Ph–Cys–Au and Ph–Cys–Au+MTX (10, 20, 30, 40, 50, 60, 70, 80, 90, and 100 μM). The non-treated cells were taken as the control. The cells were then incubated for 24, 48, and 72 hours. After treatment, 100 μL of MTT (0.5 mg mL^{-1})-containing medium was added to each well. The plates were then incubated at 37 °C with 5% CO_2 for 4 hours. The dark
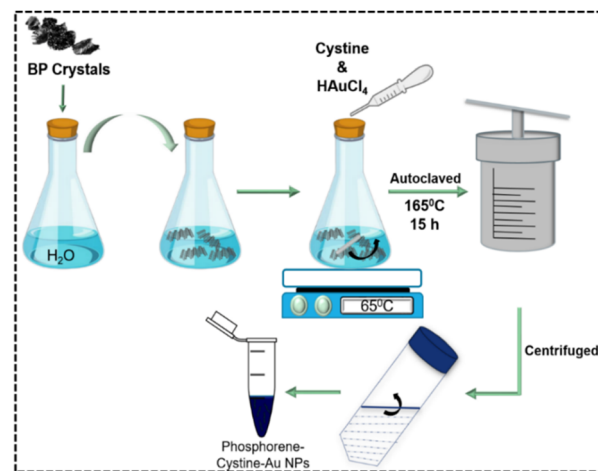
Scheme 1 Schematic representation of the synthesis of phosphorene-cystine-Au NPs from bulk BP crystals.

blue formazan crystals formed were then dissolved using DMSO for 10 minutes at room temperature to ensure complete solubilization. The absorbance of the solubilized formazan was measured at 570 nm using a microplate reader (Thermo Scientific Multiskan SkyHigh Microplate Spectrophotometer). This measurement reflects the metabolic activity and viability of the cells. Cell viability (%) was calculated using the following formula:

$$\text{Cell viability}\% = [A(\text{sample})/A(\text{Control})] \times 100$$

where A(sample) is the absorbance of the treated cells and A(Control) is the absorbance of the untreated control cells.

The obtained data were represented as means ± SD (standard deviation) from at least three independent experiments.

2.2 Characterization techniques

2.2.1 Spectroscopic analysis (UV-Vis and PL study). For the analysis of absorption spectra at room temperature, a Shimadzu UV-Vis spectrophotometer, UV-2600, was used.

The optical properties of the material were investigated using a Cary Eclipse spectrophotometer with a scan rate of about 240 nm s^{-1} and a halogen lamp source for excitation. For the analysis of fluorescence spectra, the excitation and emission spectra were obtained at a 5 nm slit with an applied voltage of 700 V. All the fluorescence measurements were carried out using quartz cells ($4 \times 1 \times 1$ cm) with vacuum Teflon stopcocks.

2.2.2 FT-IR measurements. The functional groups present in both the Ph and Ph–Cys–Au were determined by mixing the samples with KBr and obtaining the spectra using a PerkinElmer Fourier transform infrared (FT-IR) spectrophotometer. The measurements were carried out in transmission mode over 32 scans.

2.2.3 XRD characterization. For the study of phase variants and crystallinity of the synthesized material, PXRD analysis was performed on a Bruker AXS (Model D8 Advance) with Cu

Kα radiation (λ = 1.54 Å), at a scan rate of 0.5 s per step and an angular range of 2θ = 10–90°; the tube current and voltage were maintained at 40 mA and 40 kV, respectively.

2.2.4 TEM analysis. The surface morphology was studied using a transmission electron microscope, TEM-2100, from JEOL by drop casting the materials on a 3 mm Cu grid coated with carbon film and maintaining air-free conditions.

2.2.5 TRPL study. The lifetime dependency of the samples was determined using an FSP920 Edinburg Instrument, Picosecond Time-resolved cum Steady State Luminescence Spectrometer. An LED source of wavelength 375 nm was used as the excitation source.

2.2.6 DLS measurements. The zeta potentials of the samples were determined using a Malvern NanoZS90 in a glass cuvette with a square aperture and a zeta dip cell electrode at room temperature.

3. Results and discussion

3.1 Morphological and structural analysis of the synthesized Ph–Cys–Au NPs

The structural and morphological analysis of prepared Ph–Cys–Au was carried out with the help of different analytical techniques as discussed below.

Fig. 1(a and b) shows the characteristic UV-Vis peaks of phosphorene and phosphorene, cystine, and gold nanoparticles. The absorbance spectra of the synthesized composite were in the range of 200–700 nm. A sharp absorption peak was observed at 213 nm, which might be related to the structure of phosphorene. Au NPs had a prominent peak at about 550 nm that is regarded as a characteristic absorbance peak.[39] There was also a peak at 304 nm, which is a characteristic peak of cysteine. The spectrum of the Ph–Cys–Au NPs composite showed three prominent peaks for Ph, Cys, and Au NPs. The absorption peak in the visible region was weakened and presented a plateau. This confirmed that the composite is comprised of three components.[40]

In Fig. 1(c), the FTIR spectrum of phosphorene shows a prominent peak at 3426 cm^{-1}, corresponding to –OH stretching vibrations. The material also exhibited P–O–H stretching and bending at 2438 cm^{-1} and 1634 cm^{-1}, respectively. Apart from that, 1162 cm^{-1} and 1010 cm^{-1} peaks were observed for P=O and P–O, respectively.[41] However, in the case of the Ph–Cys–Au composite (Fig. 1(d)), it exhibited characteristic peaks at 3437 cm^{-1}, 2924 cm^{-1}, and 2854 cm^{-1}, corresponding to –OH stretching, asymmetric –CH stretching, and symmetric –CH stretching, respectively. They also exhibited different characteristic peaks, where 1634 cm^{-1} corresponds to –COO$^-$ stretching and P–O–H stretching, 1401 cm^{-1} corresponds to symmetric –COO$^-$ stretching and –NH in-plane stretching, 1119 cm^{-1}, 998 cm^{-1}, and 864 cm^{-1} correspond to P=O, P–O, and P–N bonds, respectively.[42,43] There were also peaks at 668 cm^{-1} and 536 cm^{-1}, which correspond to C–S and S–S stretching, respectively.[44]

As shown in Fig. 1(e and f), the X-ray diffraction analysis was performed to study the structural morphologies of Ph crystals and Ph–Cys–Au composites. The liquid exfoliated Ph nanosheets (Fig. 1(e)) showed sharp peaks at 2θ = ~16.830° for the (002) plane, ~34.118° for the (004) plane, and ~52.242° for the (006) crystal plane, which are in accordance with previous studies and match the standard pattern for BP (JCPDS No. 73-1358).[28] The obtained d-spacings were 2.265, 2.62, and 1.749 Å, corresponding to (002), (004), and (006) crystallographic planes of Ph, respectively.[45] After the hydrothermal treatment of exfoliated Ph with cystine and HAuCl$_4$, the phosphorene sheets were reduced, and a 2θ value of about 24.84° was observed, which confirmed the composite formation of Ph–Cys–Au (Fig. 1(f)).[46]

As shown in Fig. 2, for the morphological analysis, we analyzed the transmission electron microscopic images of Ph and Ph–Cys–Au nanospheres. Fig. 2(a and b) confirms the formation of sheets on the scale of 200 nm and 500 nm as per earlier studies.[47] Upon being treated with cystine and HAuCl$_4$, the sheets broke down to form nanoparticles, which can be seen from the transmission electron microscopic images as shown in Fig. 2(c and d).

We also conducted the elemental mapping of the elements present in Ph–Cys–Au, *i.e.*, P, Au, C, N, and S, using a field emission-scanning electron microscope (SIGMA VP FESEM, ZEISS) as shown in Fig. S1 in the ESI.†

Atomic force microscopy (AFM) was also conducted on exfoliated phosphorene in H$_2$O as shown in Fig. S2 (ESI).† The AFM images were obtained at 1 μm × 1 μm and 2 μm × 2 μm

Fig. 1 UV-Vis spectra of (a) Ph and (b) Ph–Cys–Au. FT-IR spectra of (c) Ph and (d) Ph–Cys–Au. XRD patterns of (e) Ph and (f) Ph–Cys–Au.

Fig. 2 (a and b) Transmission electron microscopy images of Ph nanosheets (200 nm and 500 nm); (c and d) nanospheres of Ph–Cys–Au (10 nm and 20 nm).
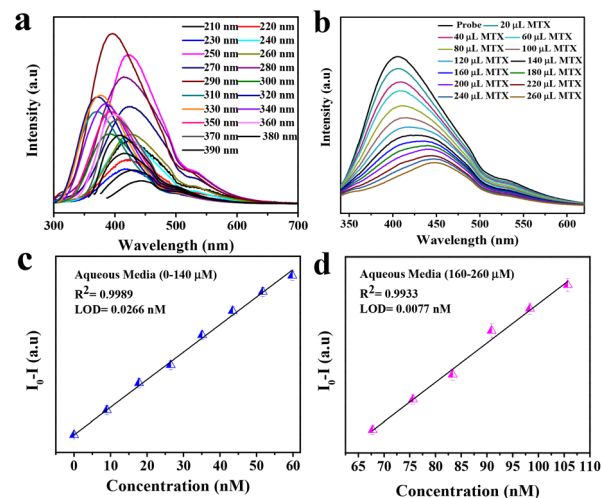

Fig. 3 (a) Fluorescence emission spectra of Ph–Cys–Au; (b) the quenching efficiency of Ph–Cys–Au concerning the concentration of methotrexate. (c) Calibration plot of turn-off sensing in the range 0–140 μL. (d) Calibration plot of turn-off sensing in the range 160–260 μL.

scales for different shapes and sizes. We carried out the analysis by drop-casting on a glass slide. We also analysed the height profile and it was observed that in the case of the 2 μm × 2 μm scale, the average thickness was about 60.5 nm. However, in the case of the 1 μm × 1 μm scale, the average thickness was about 45 nm.

3.2 Sensing experiments

3.2.1 Optical properties of the synthesized material. The optical properties of the synthesized material were analyzed by using UV-Vis absorption spectra and fluorescence measurements. The material exhibited three distinct peaks at 213 nm, 304 nm, and 550 nm, which correspond to phosphorene, cystine, and gold, due to the successful synthesis of Ph–Cys–Au nanoparticles (as shown in Fig. 1(b)). In the absence of the analyte, *i.e.*, MTX, the material showed high fluorescence intensity. The optimum optical emission for the material was observed at 396 nm at the excitation wavelength of 290 nm. The emission spectra of the synthesized material *i.e.*, Ph–Cys–Au, are shown in Fig. 3(a). The digital images before and after sensing are shown in the ESI (Fig. S3).†

The synthesized material has a very high fluorescence intensity and it showed an eventual decrease in the fluorescence intensity when the desired analyte was present. These fluorescence-based sensors are very useful for visual detection and they are practically more applicable. The real sample analysis was also carried out in the case of human blood serum (HBS) and artificial urine (AU) to check the practical applicability in the linear range of 0 to 260 μL. We also calculated the change in concentration after adding different concentrations of MTX, and it was found to be in the range of 9–105.69 μM. Fig. 3(b) shows the quenching of the probe intensity with an increase in the concentration of MTX. We also plotted the cali-

bration curve (Fig. 3c and d) to determine the LOD using the following equation:

$$LOD = 3.3 \times RSD/slope$$

It was found that the LODs in the case of aqueous media were 0.0266 nM and 0.0077 nM for the linear range (0–260 μL). For real samples such as artificial urine (AU) and human blood serum (HBS), we carried out the same experimental procedures and found that the LODs were 0.0734 nM and 0.0914 nM, respectively. This implies that Ph–Cys–Au is not only suitable for the detection of MTX in aqueous media but also in real samples.

We also calculated the limit of quantification using the following equation:

$$LOQ = 10 \times RSD/slope$$

Using the equation above, we obtained the LOQ values for aqueous media, as well as those of the real samples. The values obtained for aqueous media were 0.0807 nM (for a linear range 0–140 μL) and 0.0234 nM (for a linear range 160–260 μL), whereas, for real samples HBS and AU, the values were about 0.2771 nM and 0.2226 nM, respectively.

Apart from the LOD and LOQ, we also calculated the quantum yield of the synthesized material, which was found to be about 26.17%. The quantum yield of the fluorophore was determined with the help of an existing procedure, where we took quinine sulphate as a reference.[48] Firstly, quinine sulphate was dissolved in H_2SO_4 (0.1 M). H_2SO_4 has a refractive index of $\eta = 1.33$. The solvent used for the material synthesis was deionized water with a refractive index of $\eta = 1.33$. The fluorescence spectra were recorded with an excitation wavelength of about 290 nm. The obtained data were plotted, and the slopes for the reference and the fluorophore were deter-

mined. After that, by using the following equation, we calculated the quantum yield:

$$\varphi = \varphi_r \left(\frac{\text{Grad}}{\text{Grad}_r}\right)\left(\frac{\eta}{\eta_r}\right)^2$$

where φ is the quantum yield of the material, φ_r is the quantum yield of quinine sulphate, η is the refractive index of the deionized water, η_r is the refractive index of H_2SO_4.

3.2.2 Effect of pH. To evaluate the optimum conditions for the fluorescence turn-off property, we checked the fluorescence intensities in the presence and absence of the analyte of choice, *i.e.*, MTX (10 μM) ranging from 1.0 to 12 as shown in Fig. S4 (ESI).† The relative fluorescence intensity increased with an increase in pH ranging from 1–7. However, pH ranging from 8–12 did not show any significant change. Thus, the maximum fluorescence intensity occurred between pH 7 and 8.

3.2.3 Effect of temperature. To check the effect of temperature, we carried out the experiment with and without an analyte in the temperature range of 15–60 °C. It was observed from the bar diagram that with an increase in the temperature, the intensity value gradually decreased (Fig. S5(a)†). We also plotted the calibration graph at different temperatures, as shown in Fig. S5(b) (ESI).†

3.2.4 Stern–volmer and TRPL studies. For a better and deeper understanding of the route taking place in the case of the PL quenching phenomenon, we have analyzed the Stern–Volmer (SV) plot (Fig. 4) using the following equation:

$$I_0/I = 1 + K_{sv}[Q]$$

where, I_0 and I are the intensities of the probe before and after the addition of the quencher $[Q]$, respectively, and K_{sv} is the Stern–Volmer bimolecular binding constant. Fig. 4(a) shows the polynomial fitting of $(I_0 - I)/I$ *vs.* concentration. This equation foretells the occurrence of a dynamic or excited state energy transfer quenching mechanism or static or ground state stable complex formation in the system. The binding constant K_{sv} was calculated and found to be 0.00671, whereas the regression constant was found to be 0.9979. It has been observed from the graph that at lower concentrations, the SV plot is almost linear (Fig. 4(b)) and becomes concave with higher concentrations of the quencher. The nonlinear SV plot indicates energy transfer at the excited state, or excited state

interaction mechanism, or that the synergistic effect of the ground state mechanism is at work. At higher concentrations, a non-fluorescent ground state complex is formed as a result of a mixture of dynamic and static quenching. The complex formation is also evident from the shift as well as the new peak formation observed in the case of UV spectroscopy, as shown in Fig. S6 (ESI).†

To differentiate between dynamic and static quenching and to gain more insight into the mechanism, a TRPL study was carried out. Fig. S7† in the supplementary file shows the TRPL spectra of the probe in the presence and absence of an analyte, *i.e.*, MTX. The PL lifetime of the material changed in the presence of the analyte, which suggests dynamic quenching *via* electron transfer between the excited state donor atom and the acceptor. The χ^2 value for the probe was found to be 2.4 ns, whereas, in the presence of the analyte, this lifetime decreased to 1.9 ns, which favours dynamic quenching.

4. Mechanistic insight into the sensor

The mechanism associated with fluorescence-based sensing can be evaluated with the help of the Stern–Volmer plot and TRPL study. The general mechanisms that have been employed with fluorescence-based sensors are the IFE, PET, ACQ, and FRET. In this case, the main driving force responsible for quenching is the FRET that is taking place and this can be confirmed using different experimental evidence. In FRET, the light emitted by the fluorophore, *i.e.*, the probe, is absorbed by the analyte, which causes fluorescence quenching. This can be confirmed by the overlap of the emission spectrum of the fluorophore with the absorption spectrum of the quencher, as shown in Fig. S8 (ESI).† In this case, Ph–Cys–Au acts as a donor, and MTX acts as an acceptor, as shown in the figure. We have also calculated the overlapping area between the emission spectrum of the probe and the UV-visible spectrum of the analyte, and it was found to be about 33.293, which confirms the energy transfer between the probe and the analyte. The presence of FRET was further confirmed by the TRPL spectra, as shown in Fig. S7 (ESI).† As discussed earlier, the lifetime of the acceptor decreases as compared to the donor atom. The FRET efficiency of the system can be determined using the following equation:

$$E = 1 - (\tau_{DA}/\tau_D)$$

where τ_D is the fluorescence lifetime of the donor and τ_{DA} is the fluorescence lifetime of the donor–acceptor combination.

Using the above equation, we calculated the FRET efficiency, which was found to be about 0.2083 (20.83%). This FRET efficiency signifies the interaction between the fluorophore and the acceptor molecule as shown in Scheme 2.

4.1 Interaction

There are several mechanisms associated with FRET, and one of them is the electrostatic interaction. For FRET to occur, the donor fluorophore, as well as the acceptor molecule, must be
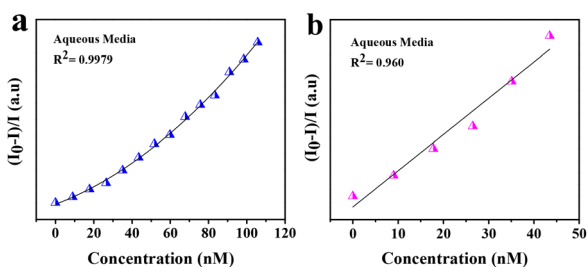

Fig. 4 Stern−Volmer plots of turn-off sensing in the range 0−260 μL in aqueous media: (a) polynomial fit and (b) linear fit.

**Scheme 2** Schematic representation of the interaction of the probe with the analyte *via* the FRET mechanism.

in close proximity, which will then lead to the electrostatic interaction. The measurement of zeta potential values in aqueous media in Fig. S9 (ESI†) showed the potential value of −27.2 eV and −25.3 eV for Ph and Ph–Cys–Au, respectively. After the interaction of Ph–Cys–Au with MTX, the potential value decreased to −18.3 eV. This prominent change in the zeta potential value corresponds to the accumulation of charge. Therefore, we can say that the interaction between the donor and the acceptor molecule is electrostatic.

The fluorescence quenching can also be confirmed from the H-bonding which can be done by the analysis of FTIR spectra between the quencher and the probe as shown in Fig. S10 (ESI).†[49] Due to the presence of electron-withdrawing groups in methotrexate (MTX), such as –COOH, –CONH–, and –NH₂ groups, they can readily form H-bonding with the functional group present in the probe. All the peaks that were present in the fluorophore remain unchanged. Among all the peaks, some of them show a minor shifting while in interaction with the quencher, which suggests H-bonding. However, two of the peaks, *i.e.*, 1401 cm^{-1} and 1119 cm^{-1}, changed to 1385 cm^{-1} and 1094 cm^{-1}, respectively. The 1385 cm^{-1} and 1094 cm^{-1} peaks correspond to the –NO and –CH groups, which means that there may be an interaction between the P–OH and –COO^{-} groups present in the fluorophore and the –NH₂ group present in the analyte. The peaks that were changed are listed in Table S1 (ESI).†

5. Interference study

One of the key characteristics of the ideal sensor is its sensitivity and selectivity towards the specific analyte of choice, even in the presence of other interfering molecules. We have investigated the PL intensity with several antibiotics, certain amino acids, and some ions that can interfere to establish the selectivity of the created system. In the case of antibiotics, we have taken amoxicillin trihydrate (AMOT), azaerythromycin (AZAE), cephalothin sodium salt (CF), cephalexin hydrate

(CFL), chloramphenicol (CFP), cefuroxime sodium salt (CFR), colistin sulphate (CLS), cloxacillin sodium (CSX), ivermectin (IVM), nalidixic acid (NA), penicillin sodium salt (PNL), streptomycin sulfate (STM), ursodeoxycholic acid (UDCS), and vancomycin (VNC) to check their efficacy for the sensor as shown in Fig. S11(a) (ESI).† Apart from these antibiotics, we have also checked the efficacy with some commonly found interfering molecules in real samples, such as aspartic acid, alanine, glycine, glutamic acid, serine, proline, ascorbic acid, Na^{+}, K^{+}, NH₄$^{+}$, and Cl^{-}. We observed that the developed sensor system is very selective towards MTX, irrespective of any other interfer-
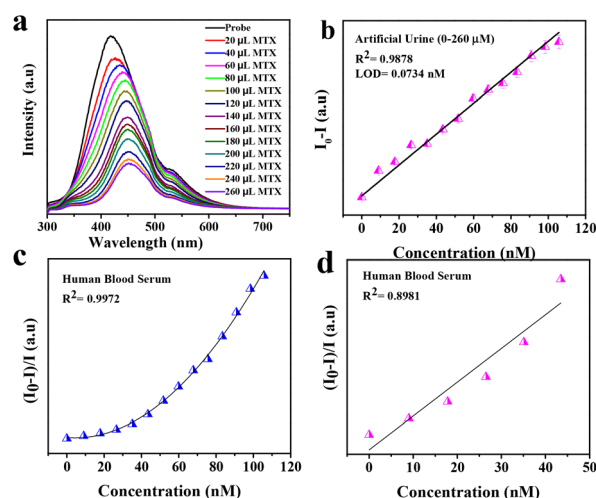
Fig. 5 (a) Quenching efficiency of the probe concerning the concentration of MTX in artificial urine (AU). (b) Calibration plot of turn-off sensing in the range 0−260 μL. (c and d) Stern−Volmer plots of turn-off sensing for AU media.
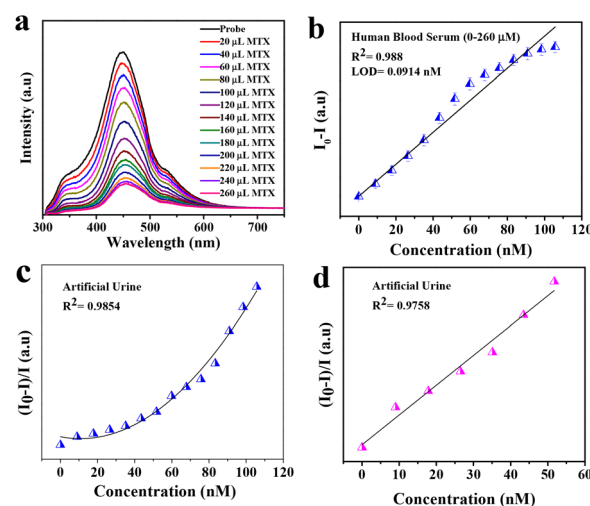
Fig. 6 (a) Quenching efficiency of the probe concerning the concentration of MTX in human blood serum (HBS). (b) Calibration plot of turn-off sensing in the range0−260 μL. (c and d) Stern−Volmer plots of turn-off sensing for HBS media.

Table 1 Recovery rates of human blood serum and artificial urine spiked with different concentrations of MTX

Real samples	Sl No.	Spiked (µM)	Found (µM)	Recovery (µM)	RSD
Artificial urine	1	20	20.76	103.8	0.010697
	2	40	43.14	107.85	0.015426
	3	60	58.97	98.28	0.005309
	4	80	83.63	104.53	0.007002
	5	100	103.55	103.55	0.002583
	6	120	119.20	99.33	0.001122
	7	140	133.34	95.24	0.00221
	8	160	160.23	100.14	0.005273
	9	180	181.21	100.67	0.006312
	10	200	195.36	97.68	0.009779
	11	220	226.64	103.01	0.002315
	12	240	239.99	99.99	0.00576
	13	260	255.95	98.44	0.001388
Human blood serum	1	20	22.04	100.18	0.008715
	2	40	36.59	91.47	0.006302
	3	60	61.23	102.05	0.004274
	4	80	85.04	106.3	0.002385
	5	100	116.18	116.18	0.001954
	6	120	148.07	123.39	0.006043
	7	140	169.25	120.89	0.002919
	8	160	184.83	115.51	0.002302
	9	180	192.71	107.06	0.002097
	10	200	205.84	102.92	0.007148
	11	220	214.35	97.43	0.001922
	12	240	221.61	92.33	0.00481
	13	260	223.86	86.10	0.005827

ing agents such as antibiotics, amino acids, and ions. Fig. S11 (b and c) in the ESI† displays bar diagrams with these results.

6. Real sample analysis

Generally, an MTX value above 10 µM is very dangerous for a period of 10 hours.[6] The practical applicability of the synthesized material has been investigated by PL quenching efficiency in real samples such as artificial urine (AU) and human blood serum (HBS), as shown in Fig. 5 and 6.[50] Using the calibration curve methods, the simultaneous determination of LOD in AU and HBS was accomplished by spiking various amounts of analyte ranging from 0–260 µL. The trends

observed in both cases can be correlated to the results obtained in the case of the aqueous media. In both cases, the fluorescence efficiency decreases effectively with an increase in the analyte volume, as observed in Fig. 5(b) and 6(b). From the calibration curve, we calculated the LOD values for both media and they were found to be about 0.0914 nM and 0.0734 nM for HBS and AU, respectively. Along with LOD, we also calculated the LOQ values, which were found to be about 0.2771 nM and 0.2226 nM for HBS and AU, respectively. Further, to check the mechanism, we plotted the Stern–Volmer curve and observed similar trends just like the aqueous media, as shown in Fig. 5 (c & d) and 6(c & d) to confirm that, in this case, the FRET mechanism is also at work.

To determine the relative standard deviation (RSD), we carried out three consecutive measurements. To assess the accuracy of this method, we determined the recovery rate of the spiked amount, which was found to be in the ranges of 95.24–107.85% and 91.47–123.39% in the case of AU and HBS, respectively. As shown in Table 1, the RSD from 0.188% to 1.5426% and 0.1922% to 0.8715% for AU and HBS, respectively, indicate the high sensitivity and reliability of the sensor for the detection of MTX in real samples. Therefore, it can be inferred from these measurements that the current system is not only applicable to an aqueous media but is also equally effective for real samples.

7. Comparative study

In the literature, there are various techniques for MTX detection. However, our synthesized sensor has numerous advantages that make it a potential material of choice for the detection of MTX. The following are the primary benefits of our work:

1. *Cost-effective*: Fluorescence-based measurements do not require any sophisticated instrument facility. The detection method is simple and does not involve complicated steps, ensuring practical applicability. Our sensor outperforms all the currently available existing sensors based on its effectiveness, sensitivity, and cost. In addition, in electrochemical analysis, strips used for the detection of bio-molecules are employed with some expensive electrochemical cells with

Table 2 A comparative study of reported sensors with our sensor

Materials	Methods	Linear range	LOD	Ref.
S, N Co-doped carbon QDs	Optical	1–300 µM L^{-1}	0.33 µM L^{-1}	51
AgNPs	SPRS	5–150 µM L^{-1}	2.1 µM L^{-1}	1
Amine-functionalized silica carbon polymer dots (APTES-CPDs)	Fluorescent	10–2.0 µg mL^{-1} and 2.0–50 µg mL^{-1}	10 ng mL^{-1} and 2.0 µg mL^{-1}	52
Au-Capped NP	Electrochemical	0.43–2 µM 1.81–5 µM	0.13 µM 0.55 µM	3
Au NPs (core-shells satellite microspheres (CSSM)-modified capillaries)	Electrochemical	0.1 nM–110 nM	—	53
Modified Ag substrate	SERS	1×10^{-16}–1×10^{-6} mol L^{-1}	1×10^{-16} mol L^{-1}	54
Poly(ʟ-cysteine)/g-C$_3$N$_4$	Electrochemical	7.5–780 µM	0.11841 µA µM^{-1} and 6 nM	55
Ph–Cys–Au	Fluorescence	0–260 µL	0.0266 nM (0–140 µM) and 0.0077 nM (160–260 µM)	This work

imprinted electrodes; our approach is cost-effective as it does not involve the use of enzymes.

2. *Appreciable detection limit*: The synthesized Ph–Cys–Au composite is effective for the detection of MTX with a detection limit of about 0.0266 nM (0–140 μL) and 0.0077 nM (160–260 μL) in a linear range of 0–260 μL.

3. *Efficacy toward real samples*: This fluorescence-based measurement is also applicable for the analysis of real samples, such as HBS and AU. The corresponding detection limits for HBS and AU are 0.0914 nM and 0.0734 nM, respectively. Our biosensor was compared with other reported sensors for the detection of MTX and is listed in Table 2 below.

8. Cytotoxicity screening

The cytotoxicity of Ph–Cys–Au and Ph–Cys–Au+MTX on Caco-2 and L-929 cell lines was investigated by treating the cells with
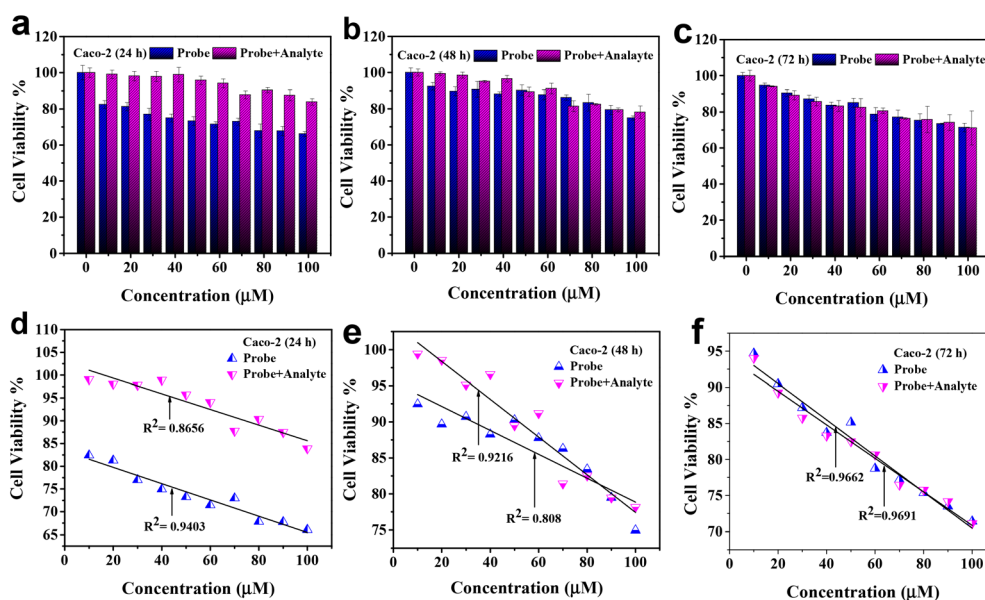

Fig. 7 (a), (b), and (c) represent the cell viability % of Caco-2 cell lines in the concentration range 10−100 μM without and with the analyte; (d), (e), and (f) show the calibration graphs for the same for incubation times of 24 h, (b) 48 h, and 72 h.

Fig. 8 (a), (b), and (c) represent the cell viability % of L-929 cell lines within the concentration range 10−100 μM without and with the analyte; (d), (e), and (f) show the calibration graph for the same for incubation times of 24 h, (b) 48 h, and 72 h.
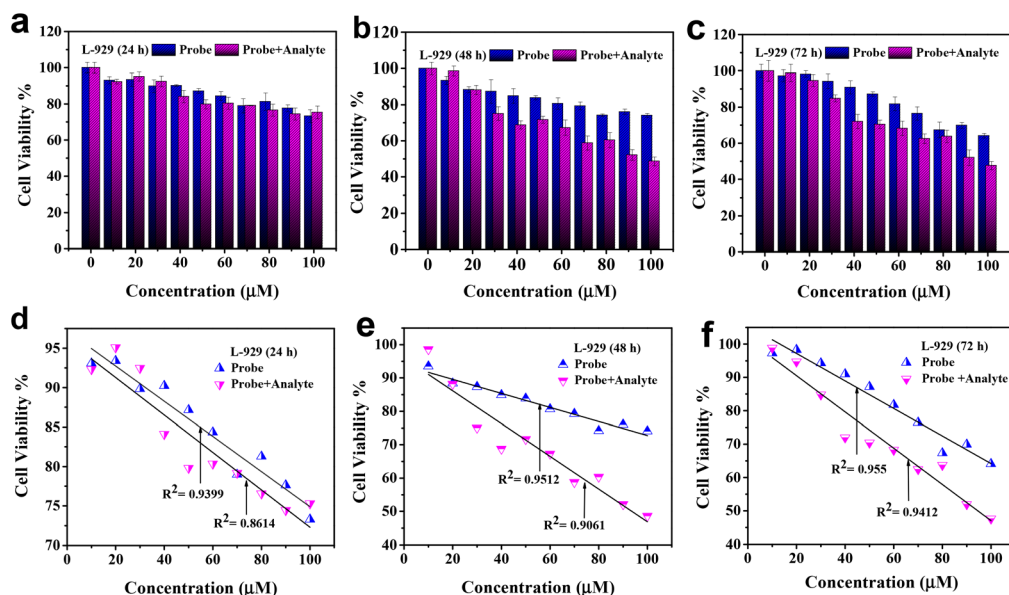
increasing concentrations (10, 20, 30, 40, 50, 60, 70, 80, 90, and 100 μM) for different periods, *i.e.*, 24, 48, and 72 hours, respectively, as shown in Fig. 7 and 8.

In the case of the Caco-2 cell line, Ph–Cys–Au exhibited toxicity at a concentration above 80 μM after 24 hours of treatment <70% (Fig. 7(a)). However, no toxicity was observed toward the Caco-2 cell line for Ph–Cys–Au after 48 and 72 hours (Fig. 7(b and c)) of treatment. On the other hand, Ph–Cys–Au+MTX did not show any toxicity to the Caco-2 cell line, regardless of the concentration or treatment duration. Fig. 7(d, e and f) shows the calibration curves.

In contrast, the L-929 cell line exhibited different responses to Ph–Cys–Au and Ph–Cys–Au+MTX. Ph-Cys-Au showed toxicity, resulting in decreased cell viability, only at a concentration above 80 μM after 72 hours (Fig. 8(c)) of treatment. However, no toxicity was observed for Ph–Cys–Au at 24 h and 48 h of treatment in the L-929 cell line (Fig. 8(a and b)). On the other hand, Ph–Cys–Au+MTX showed toxicity to the L-929 cell line at lower concentrations and earlier time points. Specifically, Ph–Cys–Au+MTX displayed toxicity at a concentration as low as 40 μM after 48 h and 72 h of treatment in the L-929 cell line (Fig. 8(b and c)). Fig. 8(d, e and f) shows the calibration curves for the same.

These results indicate that the probe has a cytotoxic effect on the Caco-2 cell line at higher concentrations and shorter treatment durations, and it seems that Caco-2 neutralized its toxicity after 48 h and 72 h of treatment. However, the Probe + analyte did not exhibit cytotoxicity toward this cell line. In contrast, the probe showed cytotoxicity in the L-929 cell line only after prolonged treatment at higher concentrations. Probe + analyte, on the other hand, demonstrated toxicity in the L-929 cell line at lower concentrations and earlier time points. The observed cytotoxicity patterns suggest that the response to the probe and probe + analyte is dose- and cell-line-dependent. It is important to consider these differences in cytotoxicity when evaluating the potential use of Ph–Cys–Au and Ph–Cys–Au+MTX in therapeutic applications. Further investigations are necessary to elucidate the underlying mechanisms of the observed cytotoxic effects and to assess their selectivity and specificity in different cell types.[56]

9. Conclusion

Herein, we report a one-step synthesis of Ph–Cys–Au from precursors black phosphorus, cystine, and $HAuCl_4$ using a simple hydrothermal process. Characterization was done using different analytical methods such as UV-visible spectroscopy, FTIR spectroscopy, PXRD, TEM, *etc.* We have introduced an effective FRET-based quenching approach to detect the anti-cancer drug methotrexate in aqueous media as well as in real samples such as human blood serum (HBS) and artificial urine (AU), making it suitable for practical applicability. This approach is cost-effective and selective as compared to other traditional methods. In aqueous media, the limits of detection of about 0.0266 nM (for a linear range of 0–140 μL) and 0.0077

nM (for a linear range of 160–260 μL) were achieved. The proposed sensing platform can effectively detect MTX in real samples. It showed a limit of detection of about 0.0734 nM and 0.0914 nM in the case of AU and HBS, respectively. Thus, we can conclude that our developed material can detect MTX in aqueous media, as well as real samples.

The noted cytotoxicity patterns imply that the responses to Ph–Cys–Au and Ph–Cys–Au+MTX depend on the dose and the cell lines used. Thus, to assess the potential therapeutic applications of Ph–Cys–Au and Ph–Cys–Au+MTX, it is crucial to take these variations into account. It is necessary to conduct additional studies to determine the underlying factors of the reported cytotoxic effects as well as their selectivity and specificity.

We hope that this information regarding the developed material, as well as the detection process, will help the scientific community to understand the properties of the emerging material and their efficiency in the field of optical sensing applications. Apart from optical sensing, the cytotoxicity assessment can help to determine how the material behaves with cancerous as well as non-cancerous cell lines, including when they come in contact with anti-cancer drugs.

Author contributions

Nasrin Sultana: conceptualization, methodology, data curation, formal analysis, writing the original draft. Chingtham Thanil Singh: contributed to experiment analysis. Mojibur R. Khan: resources, review & editing of biological analysis. Neelotpal Sen Sarma: supervision, resources, review & editing, funding acquisition.

Conflicts of interest

There is no conflict of interest.

Acknowledgements

References

1 Y. Göksel, K. Zor, T. Rindzevicius, B. E. Thorhauge Als-Nielsen, K. Schmiegelow and A. Boisen, Quantification of

methotrexate in human serum using surface-enhanced Raman scattering—Toward therapeutic drug monitoring, *ACS Sens.*, 2021, **6**(7), 2664–2673.

2 S. C. Howard, J. McCormick, C. H. Pui, R. K. Buddington and R. D. Harvey, Preventing and managing toxicities of high-dose methotrexate, *Oncologist*, 2016, **21**(12), 1471–1482.

3 Y. Goksel, E. Dumont, R. Slipets, S. T. Rajendran, S. Sarikaya, L. H. Thamdrup, K. Schmiegelow, T. Rindzevicius, K. Zor and A. Boisen, Methotrexate Detection in Serum at Clinically Relevant Levels with Electrochemically Assisted SERS on a Benchtop, Custom Built Raman Spectrometer, *ACS Sens.*, 2022, **7**(8), 2358–2369.

4 S. Jeha and C. H. Pui, in *Clinical Manifestations and Treatment of Childhood Acute Lymphoblastic Leukemia*, Elsevier Inc., 7th edn, 2018, DOI: 10.1016/B978-0-323-35762-3.00065-2.

5 B. D. Menz, S. L. Stocker, N. Verougstraete, D. Kocic, P. Galettis, C. P. Stove and S. E. Reuter, Barriers and opportunities for the clinical implementation of therapeutic drug monitoring in oncology, *Br. J. Clin. Pharmacol.*, 2021, **87**(2), 227–236.

6 I. N. Qureshi, A. Tahira, K. Aljadoa, A. M. Alsalme, A. A. Alothman, A. Nafady, A. Karsy and Z. H. Ibupoto, Polyaniline as a sacrificing template for the synthesis of controlled Co_3O_4 nanoparticles for the sensitive and selective detection of methotrexate (MTX), *J. Mater. Sci.: Mater. Electron.*, 2021, **32**(11), 15594–15604.

7 S. S. Zhao, N. Bukar, J. L. Toulouse, D. Pelechacz, R. Robitaille, J. N. Pelletier and J. F. Masson, Miniature multi-channel SPR instrument for methotrexate monitoring in clinical samples, *Biosens. Bioelectron.*, 2015, **64**, 664–670.

8 A. A. Khand, S. A. Lakho, A. Tahira, M. Ubaidullah, A. A. Alothman, K. Aljadoa, A. Nafady and Z. H. Ibupoto, Facile electrochemical determination of methotrexate (MTX) using glassy carbon electrode-modified with electronically disordered NiO nanostructures, *Nanomaterials*, 2021, **11**(5), 1266.

9 N. Salandari-Jolge, A. A. Ensafi and B. Rezaei, A novel three-dimensional network of CuCr 2 O 4/CuO nanofibers for voltammetric determination of anticancer drug methotrexate, *Anal. Bioanal. Chem.*, 2020, **412**, 2443–2453.

10 Z. Song, Y. Wang, Y. Dong, K. Xu, H. Long, C. Deng, Y. Yin, S. A. Eremin, M. Meng and R. Xi, A validated chemiluminescence immunoassay for methotrexate (MTX) and its application in a pharmacokinetic study, *Anal. Methods*, 2016, **8**(1), 162–170.

11 V. Kumar, B. Maiti, M. K. Chini, P. De and S. Satapathi, Multimodal fluorescent polymer sensor for highly sensitive detection of nitroaromatics, *Sci. Rep.*, 2019, **9**(1), 1–10.

12 R. G. Ewing, M. J. Waltman, D. A. Atkinson, J. W. Grate and P. J. Hotchkiss, The vapor pressures of explosives, *Trends Anal. Chem.*, 2013, **42**, 35–48.

13 Y. Kim, K. Giribabu, J. G. Kim, J. B. Lee, W. G. Hong, Y. S. Huh and H. J. Kim, Electrochemical sensors based on Au-ZnS hybrid nanorods with Au-mediated efficient electron relay, *ACS Sustainable Chem. Eng.*, 2018, **7**(4), 4094–4102.

14 J. He, J. Wang, M. Zhang and G. Shi, Selection of a structure-switching aptamer for the specific methotrexate detection, *ACS Sens.*, 2021, **6**(6), 2436–2441.

15 A. Inoue, Y. Ohmuro-Matsuyama, T. Kitaguchi and H. Ueda, Creation of a nanobody-based fluorescent immunosensor mini Q-body for rapid signal-on detection of small hapten methotrexate, *ACS Sens.*, 2020, **5**(11), 3457–3464.

16 B. Gogoi and N. Sen Sarma, Curcumin–cysteine and curcumin–tryptophan conjugate as fluorescence turn on sensors for picric acid in aqueous media, *ACS Appl. Mater. Interfaces*, 2015, **7**(21), 11195–11202.

17 S. S. Nagarkar, B. Joarder, A. K. Chaudhari, S. Mukherjee and S. K. Ghosh, Highly selective detection of nitro explosives by a luminescent metal–organic framework, *Angew. Chem.*, 2013, **125**(10), 2953–2957.

18 Y. Wang, L. Xiong, F. Geng, F. Zhang and M. Xu, Design of a dual-signaling sensing system for fluorescent ratiometric detection of Al^{3+} ion based on the inner-filter effect, *Analyst*, 2011, **136**(22), 4809–4814.

19 B. Liu, C. Tong, L. Feng, C. Wang, Y. He and C. Lü, Water-soluble polymer functionalized CdTe/ZnS quantum dots: A facile ratiometric fluorescent probe for sensitive and selective detection of nitroaromatic explosives, *Chem. – Eur. J.*, 2014, **20**(8), 2132–2137.

20 B. Gole, S. Shanmugaraju, A. K. Bar and P. S. Mukherjee, Supramolecular polymer for explosives sensing: role of H-bonding in enhancement of sensitivity in the solid state, *Chem. Commun.*, 2011, **47**(36), 10046–10048.

21 W. R. Algar, A. Szwarczewski and M. Massey, Are We There Yet? Intracellular Sensing with Luminescent Nanoparticles and FRET, *Anal. Chem.*, 2023, **95**(2), 551–559.

22 E. Asadian, S. Shahrokhian, A. I. Zad and F. Ghorbani-Bidkorbeh, Glassy carbon electrode modified with 3D graphene–carbon nanotube network for sensitive electrochemical determination of methotrexate, *Sens. Actuators, B*, 2017, **239**, 617–627.

23 H. Ghadimi, B. Nasiri-Tabrizi, P. M. Nia, W. J. Basirun, R. M. Tehrani and F. Lorestani, Nanocomposites of nitrogen-doped graphene decorated with a palladium silver bimetallic alloy for use as a biosensor for methotrexate detection, *RSC Adv.*, 2015, **5**(120), 99555–99565.

24 W. Zhai, Y. Chen, Y. Liu, T. Sakthivel, Y. Ma, Y. Qin, Y. Qu and Z. Dai, Enlarging the Ni–O Bond Polarizability in a Phosphorene-Hosted Metal–Organic Framework for Boosted Water Oxidation Electrocatalysis, *ACS Nano*, 2023, **17**(17), 17254–17264.

25 C. D. Zhang, J. C. Lian, W. Yi, Y. H. Jiang, L. W. Liu, H. Hu, W. D. Xiao, S. X. Du, L. L. Sun and H. J. Gao, Surface structures of black phosphorus investigated with scanning tunneling microscopy, *J. Phys. Chem. C*, 2015, **113**(43), 18823–18826.

26 A. Goswami and M. B. Gawande, Phosphorene: Current status, challenges and opportunities, *Front. Chem. Sci. Eng.*, 2019, **13**, 296–309.

27 A. Avsar, I. J. Vera-Marun, J. Y. Tan, K. Watanabe, T. Taniguchi, A. H. Castro Neto and B. Ozyilmaz, Air-stable transport in graphene-contacted, fully encapsulated ultra-thin black phosphorus-based field-effect transistors, *ACS Nano*, 2015, **9**(4), 4138–4145.

28 S. K. Tuteja and S. Neethirajan, Exploration of two-dimensional bio-functionalized phosphorene nanosheets (black phosphorous) for label free haptoglobin electro-immuno-sensing applications, *Nanotechnology*, 2018, **29**(13), 135101.

29 Y. Chen, R. Ren, H. Pu, J. Chang, S. Mao and J. Chen, Field-effect transistor biosensors with two-dimensional black phosphorus nanosheets, *Biosens. Bioelectron.*, 2017, **89**, 505–510.

30 R. Gusmao, Z. Sofer and M. Pumera, Black phosphorus rediscovered: from bulk material to monolayers, *Angew. Chem., Int. Ed.*, 2017, **56**(28), 8052–8072.

31 S. Y. Cho, Y. Lee, H. J. Koh, H. Jung, J. S. Kim, H. W. Yoo, J. Kim and H. T. Jung, Superior chemical sensing performance of black phosphorus: comparison with MoS_2 and graphene, *Adv. Mater.*, 2016, **28**(32), 7020–7028.

32 N. M. Latiff, W. Z. Teo, Z. Sofer, A. C. Fisher and M. Pumera, The cytotoxicity of layered black phosphorusm, *Chem. – Eur. J.*, 2015, **21**(40), 13991–13995.

33 H. U. Lee, S. Y. Park, S. C. Lee, S. Choi, S. Seo, H. Kim, J. Won, K. Choi, K. S. Kang, H. G. Park, H. S. Kim, H. R. An, K. H. Jeong, Y. C. Lee and J. Lee, Black phosphorus (BP) nanodots for potential biomedical applications, *Small*, 2016, **12**(2), 214–219.

34 X. Jiang, H. Jin, Y. Sun, Z. Sun and R. Gui, Assembly of black phosphorus quantum dots-doped MOF and silver nanoclusters as a versatile enzyme-catalyzed biosensor for solution, flexible substrate and latent fingerprint visual detection of baicalin, *Biosens. Bioelectron.*, 2020, **152**, 112012.

35 Y. Zeng and Z. Guo, Synthesis and stabilization of black phosphorus and phosphorene: Recent progress and perspectives, *iScience*, 2021, **24**(10), DOI: **10.1016/j. isci.2021.103116**.

36 T. Nilges, M. Kersting and T. Pfeifer, A fast low-pressure transport route to large black phosphorus single crystals, *J. Solid State Chem.*, 2018, **181**(8), 1707–1711.

37 S. Pan, J. He, C. Wang and Y. Zuo, Exfoliation of two-dimensional phosphorene sheets with enhanced photocatalytic activity under simulated sunlight, *Mater. Lett.*, 2018, **212**, 311–314.

38 M. Kandasamy, M. Selvaraj, C. Kumarappan and S. Murugesan, Plasmonic Ag nanoparticles anchored ethylenediamine modified TiO2 nanowires@ graphene oxide composites for dye-sensitized solar cellm, *J. Alloys Compd.*, 2022, **902**, 163743.

39 K. Esumi, S. Sarashina and T. Yoshimura, Synthesis of gold nanoparticles from an organometallic compound in supercritical carbon dioxide, *Langmuir*, 2004, **20**(13), 5189–5191.

40 L. Zhu, L. Xu, B. Huang, N. Jia, L. Tan and S. Yao, Simultaneous determination of Cd(ɪɪ) and Pb(ɪɪ) using square wave anodic stripping voltammetry at a gold nanoparticle-graphene-cysteine composite modified bismuth film electrode, *Electrochim. Acta*, 2014, **115**, 471–477.

41 N. Sultana, A. Degg, K. J. Goswami, B. Gogoi, T. Nilges and N. Sen Sarma, Reduced Phosphorene Quantum Dot Incorporated Flexible Bio-Electronic Device for the Detection of Uric Acid in Real Media, *ACS Appl. Electron. Mater.*, 2023, **5**(3), 1502–1513.

42 S. Ge, L. Zhang, P. Wang and Y. Fang, Intense, stable and excitation wavelength-independent photoluminescence emission in the blue-violet region from phosphorene quantum dots, *Sci. Rep.*, 2016, **6**(1), 27307.

43 S. Qiu and S. Qiu, *Air stable polyphosphazene functionalized few-layer black phosphorene for flame retardancy of epoxy resins*, Springer, 2021, pp. 33–57, DOI: **10.1007/978-981-16-3552-6_2**.

44 L. Zhu, L. Xu, B. Huang, N. Jia, L. Tan and S. Yao, Simultaneous determination of Cd(II) and Pb(II) using square wave anodic stripping voltammetry at a gold nanoparticle-graphene-cysteine composite modified bismuth film electrode, *Electrochim. Acta*, 2014, **115**, 471–477.

45 P. Vishnoi, M. Mazumder, M. Barua, S. K. Pati and C. N. R. Rao, Phosphorene quantum dots, *Chem. Phys. Lett.*, 2018, **699**, 223–228.

46 S. A. Soomro, I. H. Gul, H. Naseer, S. Marwat and M. Mujahid, Improved performance of $CuFe_2O_4/rGO$ nanohybrid as an anode material for lithium-ion batteries prepared via facile one-step method, *Curr. Nanosci.*, 2019, **15**(4), 420–429.

47 B. Tian, B. Tian, B. Smith, M. C. Scott, Q. Lei, R. Hua, Y. Tian and Y. Liu, Facile bottom-up synthesis of partially oxidized black phosphorus nanosheets as metal-free photocatalyst for hydrogen evolution, *Proc. Natl. Acad. Sci.*, 2018, **115**(17), 4345–4350.

48 M. R. Pacquiao, M. D. G. de Luna, N. Thongsai, S. Kladsomboon and P. Paoprasert, Highly fluorescent carbon dots from enokitake mushroom as multi-faceted optical nanomaterials for Cr6+ and VOC detection and imaging applications, *Appl. Surf. Sci.*, 2018, **453**, 192–203.

49 P. Dutta, D. Saikia, N. C. Adhikary and N. S. Sarma, Macromolecular systems with MSA-Capped CdTe and CdTe/ZnS Core/Shell quantum dots as superselective and ultrasensitive optical sensors for picric acid explosive, *ACS Appl. Mater. Interfaces*, 2015, **7**(44), 24778–24790.

50 Z. Chen, S. Qian, X. Chen, W. Gao and Y. Lin, Protein-templated gold nanoclusters as fluorescence probes for the detection of methotrexate, *Analyst*, 2012, **137**(18), 4356–4361.

51 X. Wei, X. Si, M. Han and C. Bai, One-Step Preparation of S, N Co-Doped Carbon Quantum Dots for the Highly Sensitive and Simple Detection of Methotrexate, *Molecules*, 2022, **27**(7), 2118.

52 Z. Golsanamlou, H. Kholafazad-Kordasht, J. Soleymani and A. Jouyban, Quantification of methotrexate in plasma samples using highly fluorescent nanoparticles, *J. Pharm. Biomed. Anal.*, 2022, **214**, 114716.

53 M. Chen, J. Tang, W. Luo, Z. Zhang, Y. Zhu, R. Wang, H. Yang and X. Chen, Core-shell-satellite microspheres-

modified glass capillary for micro sampling and ultra-sensitive SERS spectroscopic detection of methotrexate in serum, *Sens. Actuators, B*, 2018, **275**, 267–276.

54 X. Jiang, J. Zhang, L. Xu, W. Wang, J. Du, M. Qu, X. Han, L. Yang and B. Zhao, Ultrasensitive SERS detection of antitumor drug methotrexate based on modified Ag substrate, *Spectrochim. Acta, Part A*, 2020, **240**, 118589.

55 Y. Wang, S. Li, Y. Gao, B. Du, S. Vafaei, M. Li, H. Wu, X. Tong and Y. Chen, Synthesis of poly (L-cysteine)/g-C_3N_4

modified glassy carbon electrodes for electrochemical detection of methotrexate as a medicine for treatment of breast cancer in pharmaceutical fluid samples, *Chemosphere*, 2023, **331**, 138769.

56 M. Biedulska, P. Jakóbczyk, M. Sosnowska, B. Dec, A. Muchlińska, A. J. Zaczek, D. Nidzworski and R. Bogdanowicz, Cytocompatibility of stabilized black phosphorus nanosheets tailored by directly conjugated polymeric micelles for human breast cancer therapy, *Sci. Rep.*, 2021, **11**(1), 9304.